coatings

MDPI

Article

High-Velocity Oxy-Fuel (HVOF) Spray Coating of Inconel, Colmonoy, and Aluminum on AISI 316L Stainless Steel: A Comparative Investigation of the Microstructure and Corrosion Resistance of Coatings

M. Taghian [1,*], M. Heydarian [1], S. Torkian [1], M. Parham Dabir [1], A. Bahrami [1], S. H. Mousavi Anijdan [2,*] and N. Park [3,4]

1 Department of Materials Engineering, Isfahan University of Technology, Isfahan 8415683111, Iran
2 Department of Materials Engineering, Science and Research Branch, Islamic Azad University, Tehran 1477893855, Iran
3 School of Materials Science and Engineering, Yeungnam University, 280 Daehak-Ro, Gyeongsan 38541, Gyeongsangbuk-do, Republic of Korea
4 Institute of Materials Technology, Yeungnam University, 280 Daehak-Ro, Gyeongsan 38541, Gyeongsangbuk-do, Republic of Korea
* Correspondence: mtaghian71@yahoo.com (M.T.); hashemmousavi@gmail.com (S.H.M.A.)

Abstract: This study examines the effect of high-velocity oxy-fuel (HVOF) coatings of Inconel, aluminum, and Colmonoy on the corrosion resistance of stainless steel substrates. The coated samples were characterized using SEM, XRD, and EDS techniques. Impedance and Tafel tests were used to investigate the coatings corrosion responses at 40, 50, and 60 °C. Inconel-coated specimens showed superior corrosion behavior thanks to the Cr_2O_3 layers formed between the lamella structures of the coating, preventing chloride ions from diffusing across the coating. Although the Nyquist curve indicated oxide layer formation for the Al-coated sample, the Tafel test results showed severe corrosion.

Keywords: corrosion; HVOF; impedance; stainless steel

1. Introduction

Stainless steel grades are amongst the most commonly used alloying grades in marine and off-shore installations, including marine oil/gas extraction plants, underwater robots, and submarines [1–3]. Stainless steels show better corrosion resistance than carbon steels, thanks to the formation of an inherent passive oxide film on their surfaces [4,5]. Nevertheless, there are some serious concerns regarding the corrosion resistance of stainless steel in sea waters and chlorine-containing aqueous environments [6–8]. In marine environments, severe localized corrosion and pitting in stainless steel are always critical issues, especially when the temperature increases and the humidity rises. Tiny water droplets in marine atmospheres often contain high concentrations of chloride ions, i.e., they are rich in salt, creating a localized aggressive corrosive surface condition [9,10]. Several methods can be employed to enhance the corrosion resistance of stainless steel, such as cold metal transfer [11], laser surface treatment [12], and high-velocity oxy-fuel (HVOF) metal spray [13,14]. Thermal spraying of metallic and ceramic coatings has long been highly efficient in improving the properties of metallic substrates against abrasive wear, corrosion, and oxidation. That has made thermal spraying a vastly used method in many industrial sectors such as aerospace, automotive, steelmaking, and energy sectors [15–17]. Thermally sprayed coatings often have relatively low porosity and high bonding strength [18]. HVOF coating of Inconel on the stainless steel surface can reportedly significantly enhance the corrosion resistance of the stainless steel [19–21]. Moreover, it has been found that laser treatment after HVOF

makes the corrosion resistance of Inconel coating even better [22,23]. Another study found that HVOF parameters affect the coating's surface morphology, porosity, and corrosion resistance. The optimum HVOF parameters resulting in the best corrosion resistance were a spraying distance of 380 mm and a powder feed rate of 60 g/min [22]. Reportedly, the lamella microstructure of Inconel HVOF coating prevents the corroding solutions from reaching the substrate surface [14]. In another study, three coatings, including Inconel, aluminum, and AlZn, were applied on stainless steel substrate by the HVOF process, and samples were immersed in NaCl solution for 1000 h. It was found that Inconel coatings showed less delamination than other coatings, and the coating was suitable enough for a corrosion reduction rate of 0.1140 mm/year in chlorine-containing electrolytes [24].

This research further investigates the corrosion resistance of AISI 316 L, coated with Al, Colmonoy, and Inconel-625 by HVOF. The microstructure and corrosion behaviors of coated samples were studied at three temperatures.

2. Materials and Methods

The substrates used in this study were 20 cm × 20 cm AISI 316 L stainless steel plates. Three commercial powders were used for the high-velocity oxy-fuel (HVOF) process. The properties of these powders are listed in Table 1. The morphology of all powders was spherical. The substrate surface was sand-blasted before HVOF to remove surface pollution and improve bonding.

Table 1. The particle size of selected powders.

Alloy	Al	Si	Ni	B	C	Cr	Fe	Mo	Ti	Co	Mn	Particle Size (μm)
Al99	99.9	0.04	-	-	-	-	0.06	-	-	-	-	11–45
Colomonoy-6	-	4.18	73.61	2.8	0.68	13.7	4.2	-	-	-	-	20–53
Inconel625	0.11	0.18	Balance	-	0.06	21.86	3.22	8.8	0.23	0.06	0.2	11–45

The chosen HVOF parameters are shown in Table 2. The coated substrates were cut to 1 cm × 1 cm dimensions with electro-discharge machining (EDM) and cleaned with acetone in an ultrasonic bath, followed by air drying. Samples were then mounted, and after grinding and polishing, the microstructure of coated samples was studied by the Philips XI30 Scanning Electron Microscopy (SEM, Hillsboro, OR, U.S.A.) instrument. Phase characterization was carried out by X-ray diffraction (Philips X-Pert, Hillsboro, OR, U.S.A.).

Table 2. HVOF parameters.

Title 1	Fuel	Oxygen	Distance	Powder	Carrier Gas	Nozzle
	mL/min	L/mm	mm	gr/min	L/min	mm
Al99	200	800	340	35	8	100
Inconel 625	280	900	400	60	8	100
Colmonoy-6	280	800	340	60	8	100

Elemental analysis was performed by the Seron AIS2300 EDS analyzer (Uiwang, Korea). Coated samples were ground up by 1200 SiC grinding paper to study the corrosion behavior of the three chosen coatings. A three-electrode system connected to an Iviumsat instrument was used to study the corrosion behavior of coated samples. The Ag/AgCl/saturated KCl electrode, platinum electrode, and coated samples were used as reference, counter, and working electrodes, respectively. Based on the working conditions, three temperatures were chosen: 40, 50, and 60 °C. The open-circuit test was carried out before Electrochemical Impedance Spectroscopy (EIS) and Tafel tests for 3600 s. The electrolyte was 3.5% NaCl solution, and its volume for each test was 250 mL. The EIS test was performed at a frequency of 100 kHz to 10 MHz by 0.01 V amplitude; after the EIS test, the Tafel test was carried out in a voltage range of −250 mV

versus open-circuit potential to 1200 mV versus the Ag/AgCl/saturated KCl electrode with the scan rate of 1 mV/s. All results of EIS tests were analyzed by Z-View software. Every test was repeated three times. For the calculation of corrosion rates, Equation (1) was used.

$$\text{Corrosion Rate} = K\,(i_{corr} \times M)/(n \times d)$$
(K: 0.00327 for corrosion rate of mm/year);
I_{corr}: current density ($\mu A/cm^2$);
M: atomic mass;
n: number of charge transfer;
d: density (g/cm^3).   (1)

where K is a constant, here equals 0.00327 and i_{corr} denotes the current density ($\mu A/cm^2$), with M, n and d (g/cm^3) standing for atomic mass, number of charge transfer and density, respectively.

3. Results and Discussion

3.1. Coating Characterization

Figure 1 shows the X-ray diffraction (XRD) patterns of the substrate and three coatings. The γ phase is the dominant phase in AISI 316 L steel. That is, the Al99-coated sample is expectedly aluminum. In Colmonoy, a mixture of $Cr_{28}C_{12}Fe_1Ni_3$, Cr_8B_4, and γ-(Ni) was detected. In Inconel 625, Cr_2O_3 and γ-(Ni) were detected. The formation of oxides and intermetallic compounds in HVOF is highly expected due to high temperatures in the HVOF nozzle. The oxidation reactions during the HVOF process take place in three steps: (i) exposure of particles to a high-temperature atmosphere while powders are ejected from the nozzle, (ii) exposure of flying particles to the entrapped atmosphere inside the flame, and (iii) exposure of particles to the atmosphere when they are deposited over the surface. Therefore, the formation of oxide phases and Cr_2O_3 in the Inconel-coated sample is not surprising.
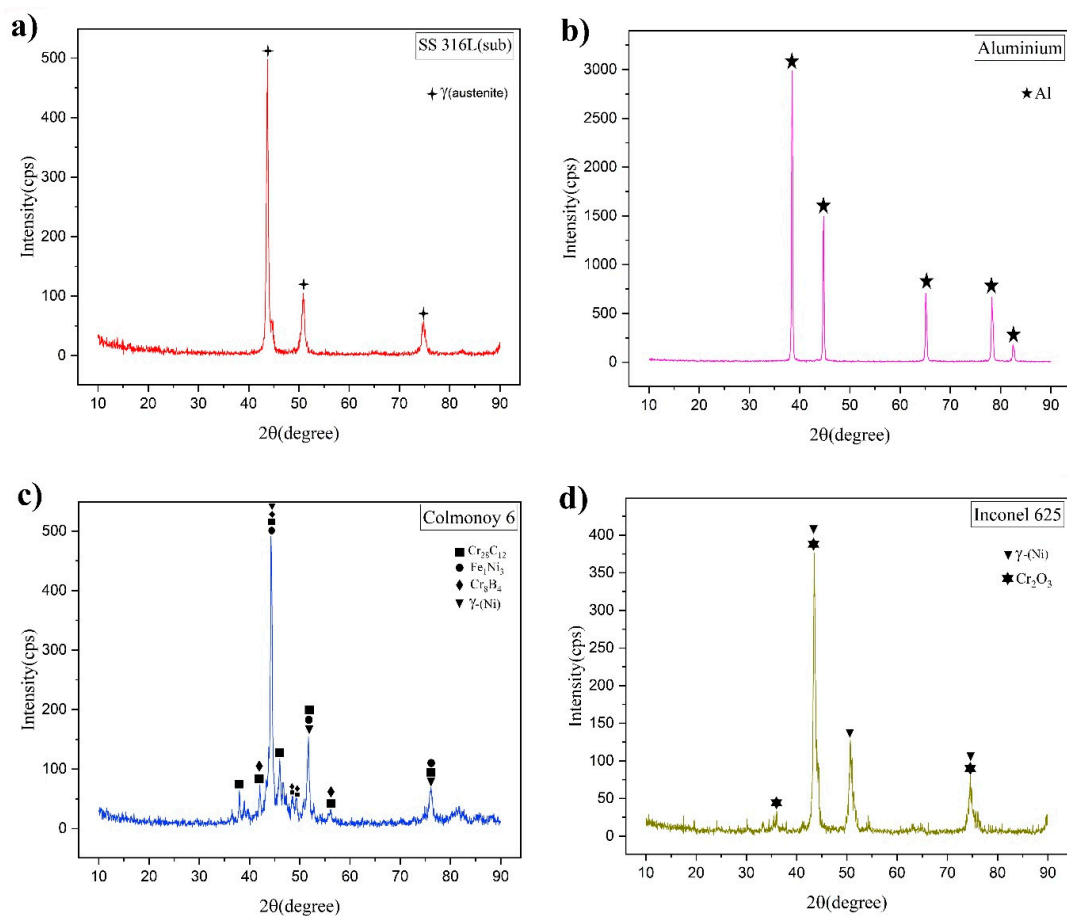

Figure 1. XRD of (**a**) SS 316 L, (**b**) aluminum, (**c**) Colmonoy-6, and (**d**) Inconel 625.

Another commonly observed characteristic feature of thermal spray coating is the formation of splats when particles hit the surface. These splats significantly contribute to the mechanical bonding of HVOF coatings to the substrate [14]. The formation of splats is seen in both optical (Figure 2) and SEM micrographs (Figure 3) of Inconel-coated samples. It is noticeable that there are continuous grayish regions in between splats (see arrows in Figure 3c). In the backscattered electron SEM mode, it was confirmed that these grayish regions are not porosities and discontinuities (see Figure 3). EDS and XRD results showed that these regions are chromium oxide layers.
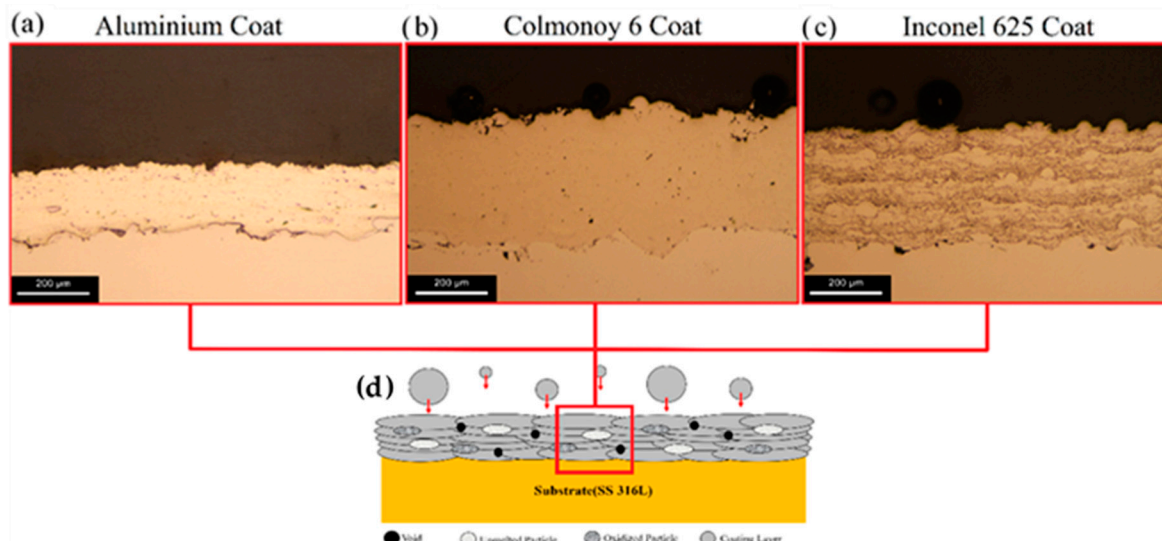

Figure 2. Optical microscope micrographs of (**a**) Al, (**b**) Colmonoy, (**c**) Inconel coatings, and (**d**) a schematic of how particles hit the surface during the HVOF process.
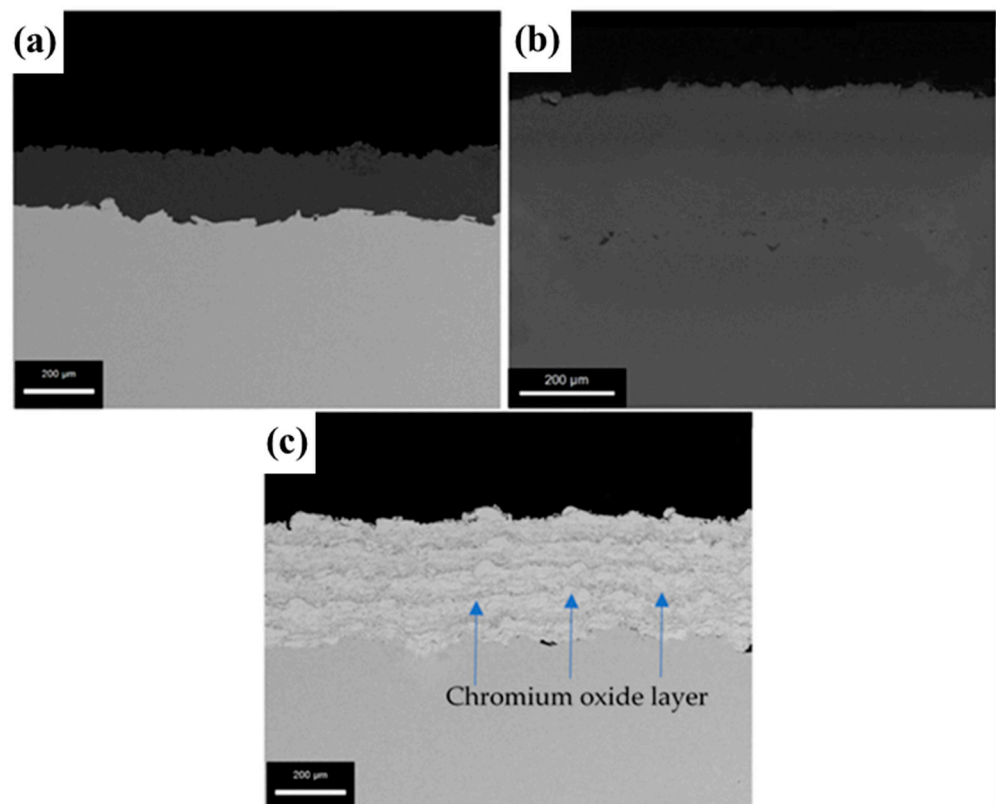

Figure 3. Scanning electron micrographs of (**a**) Al, (**b**) Colmonoy, and (**c**) Inconel coatings.

Contrary to Inconel-coated samples, continuous splats are hardly visible in Colmonoy-coated samples. In this case, it appears that discontinuous splats are dominant. In Al-coated samples, a continuous morphology is observed in the coating, possibly because of the low melting temperature and complete melting during the HVOF process.

The elemental linear analyses through Al, Inconel, and Colmonoy coating layers are depicted in Figure 4. In Al-coated samples (Figure 4a), Al, Fe, and Cr are the main elements along the analysis line. As expected, Al is the main element in the coating. In Colmonoy-coated samples, Ni, Cr, and Fe were detected alongside the analysis line (Figure 4b). Similar to other cases, alloying elements are homogeneously distributed in the substrate and the coating. Moreover, the transition from the coating to the substrate is again rather sharp, with no indication of heavy depletion/accumulation of alloying elements on either side of the interface (see Figure 4b). As depicted in Figure 4c, in Inconel-coated samples, Ni, Cr, Mo, and Fe are homogeneously distributed in the coating and the substrate. It is also clear that moving from the coating to the substrate, the intensity of the Fe peak rather sharply increases, while the intensities of Ni and Mo peaks decrease. Such a sharp transition from the coating to the substrate is an indication that a diffused interface is not formed at the substrate/coating interface. As far as Cr is concerned, the variation in the intensity is not noteworthy, as chromium exists in both the substrate and the coating (see Figure 4c).
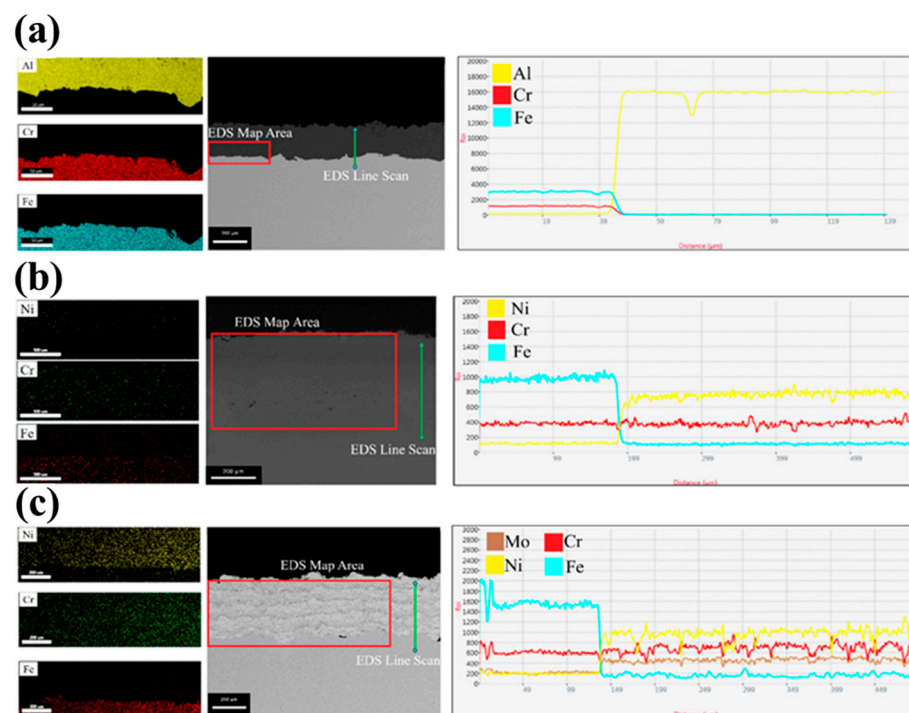

Figure 4. EDS line scan analyses of (**a**) Al, (**b**) Colmonoy, and (**c**) Inconel-coated samples.

3.2. Corrosion Results

3.2.1. Potentiodynamic Polarization

The results of electrochemical tests are depicted in Figure 5 and summarized in Table 3, where I_{corr} is the corrosion current density ($\mu A/cm^2$), E_{corr} is the corrosion potential (mV), and CR is the corrosion rate (mm/year). The highlights and essential observations are summarized as follows.
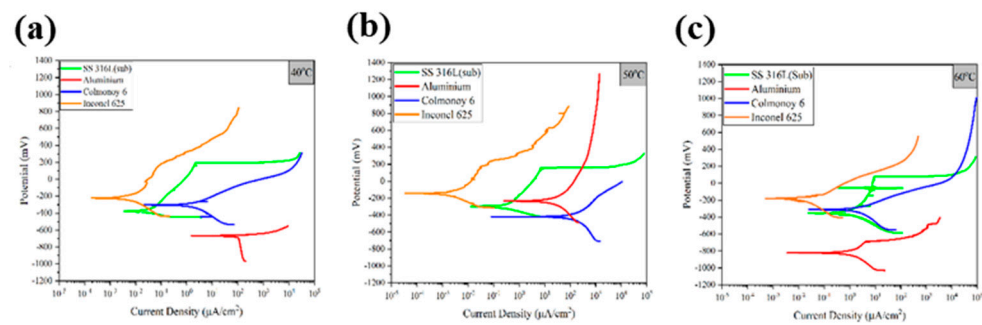
Figure 5. Polarization curves for the substrate and coatings at (**a**) 40 °C, (**b**) 50 °C, and (**c**) 60 °C.

Table 3. Summary of results of electrochemical tests.

Samples	Temp.	E_{corr}	I_{corr}	CR
	°C	mV	$\mu A/cm^2$	mm/Year
AISI 316 L		−375.6	0.03	0.000232037
Aluminum coating	40	−668.39	110.25	1.201725
Colmonoy-6 coating		−302.43	3.61	0.02792179
Inconel 625 coating		−223.93	5.5×10^{-3}	5.931×10^{-5}
AISI 316 L		−299.66	0.25	0.001934681
Aluminum coating	50	−231.96	27.66	0.301494
Colmonoy-6 coating		−420.03	72.29	0.559131919
Inconel 625 coating		−147	1.3×10^{-3}	1.4018×10^{-5}
AISI 316 L		−350.67	0.82	0.006342346
Aluminum coating	60	−825.82	0.4	0.00436
Colmonoy-6 coating		−308.6	1.92	0.014850371
Inconel 625 coating		−182.76	19×10^{-3}	0.000204889

The lowest corrosion resistance/highest corrosion rate of all test conditions was observed in the Al-coated sample at 40 °C. This is comparatively much lower than the corrosion resistance of the base alloy. The HVOF Al spray coating of the AISI 316 L substrate does not improve the corrosion resistance of the stainless steel substrate, especially at 40 and 50 °C. This can be explained by the fact that the oxidation/reduction potential of Al is lower than that of stainless steel substrate. Another observation related to Al coating worth mentioning is the effect of temperature on the corrosion rate of Al-coated specimens. It is seen that the higher the temperature, the better the corrosion resistance of the Al-coated samples, such that at 50 °C, the corrosion resistance of the Al-coated specimen is comparable (slightly better, in fact) to that of the substrate. This can be explained by the temperature-dependent formation of Al_2O_3 on Al, making a passive layer on the outer surface of the coating.

The Colmonoy-6 coating shows more or less a similar trend to the Al-coated samples, i.e., the Colmonoy coating ends up in samples with comparatively lower corrosion resistance when compared to the base alloy. Although Colmonoy outperforms the Al coating, it is still far from an acceptable protective coating on the stainless steel base alloy in the chosen testing conditions. As explained earlier in the manuscript, the Colmonoy coating differentiates itself from the two other samples as discontinuous splats exist in the microstructure (see Figures 2 and 3). The downside of such discontinuous microstructure is the possibility of the penetration of corrosive solutions (electrolytes) into the coating, which in turn deteriorates the corrosion resistance of the coating [18]. In addition, Colmonoy has comparatively lower chromium content than the substrate alloy, making it a less protective coating. Chromium content is an essential element for surface passivation and corrosion resistance [25]. Inconel-coated specimens show the maximum corrosion resistance of all samples at all temperatures. More importantly, contrary to Al and Colmonoy, the HVOF spray coating of Inconel on stainless steel substrate appears to significantly enhance the corrosion resistance of the base alloy (the lowest corrosion resistance of all samples is highlighted in green). According to XRD and SEM

results (see Figures 1 and 3), the Inconel coating has a lamella structure with continuous oxide (Cr_2O_3) layers present throughout the whole thickness. These continuous oxide layers act as protective barriers. This way, they can minimize the corrosive solution/electrolyte penetration down into the coating and further down to the substrate, resulting in improved corrosion resistance. Al and Colmonoy HVOF coatings showed disappointing corrosion behaviors. Therefore, they appear related to these coatings' electrochemical and morphological features.

The polarization curves of different coated samples and the base alloy are represented in Figures 6 and 7. In Al-coated samples, an increase in temperature from 40 to 50 °C is associated with a positive shift in corrosion potential. A further increase from 50 to 60 °C in this sample dramatically decreases the current density, inferring that a (thick enough) oxide layer has formed at this temperature. Corrosion of the Al-coated specimen is controlled by several concurrent factors other than the formation of the oxide layer. Reportedly, two factors came into play with an increment in temperature: (i) oxygen diffusion and (ii) oxygen solubility. While the former increases with increasing temperature, the latter shows a reverse trend. Moreover, the diffusion of other aggressive ions, such as Cl^-, increases at higher temperatures [26].
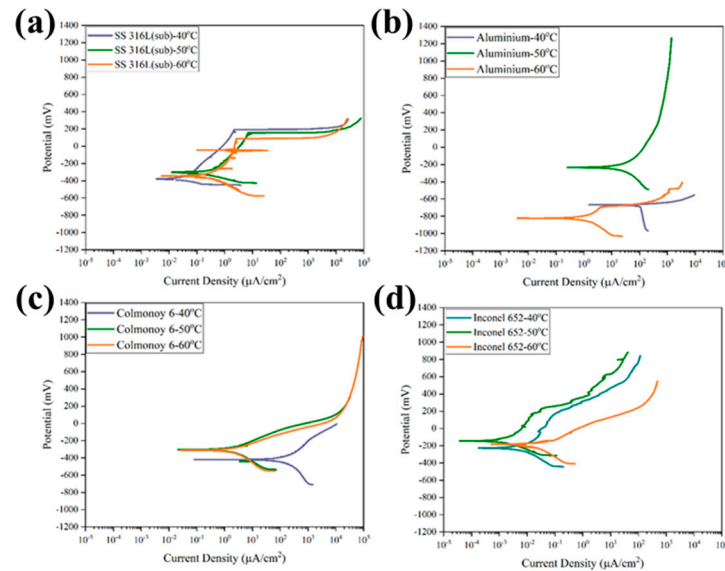

Figure 6. Polarization curves of (**a**) AISI 316 stainless steel, (**b**) Al, (**c**) Colmonoy, and (**d**) Inconel-coated samples.
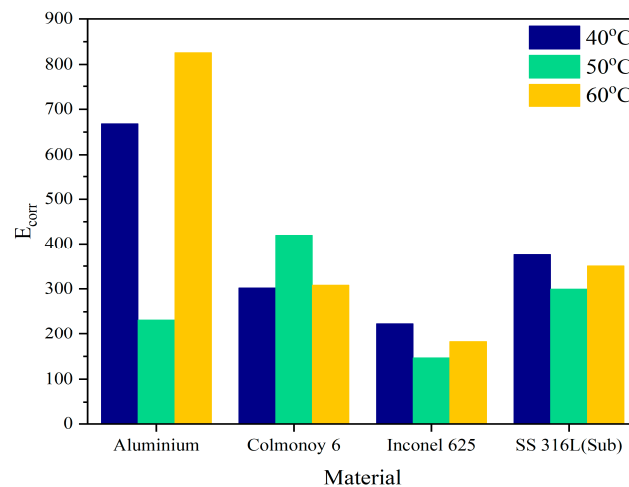

Figure 7. Potential of different coating samples at different temperatures.

From 40 to 50°C, the diffusion of chloride ions rises, and oxygen solubility decreases, making the NiO layer challenging to recover [27,28]. Increased oxygen ion penetration at 60 °C induces the production of a Cr_2O_3 oxide layer, which has high corrosion resistance and protects the coating with a barrier mechanism, improving the corrosion resistance of the Colmonoy coating at 60 °C compared to 50 °C. For the Inconel-coated specimens, the minimum corrosion current density is attained at 50 °C, while the lowest (most negative) corrosion potential is observed at 60 °C. For this sample, we observed a slight deterioration in corrosion behavior at 60 °C, attributed to the higher/easier diffusion of Cl and oxygen ions at this temperature [26]. Figures 7–9 represent important corrosion parameters, showing that overall, Inconel-coated specimens outperformed the other coatings.
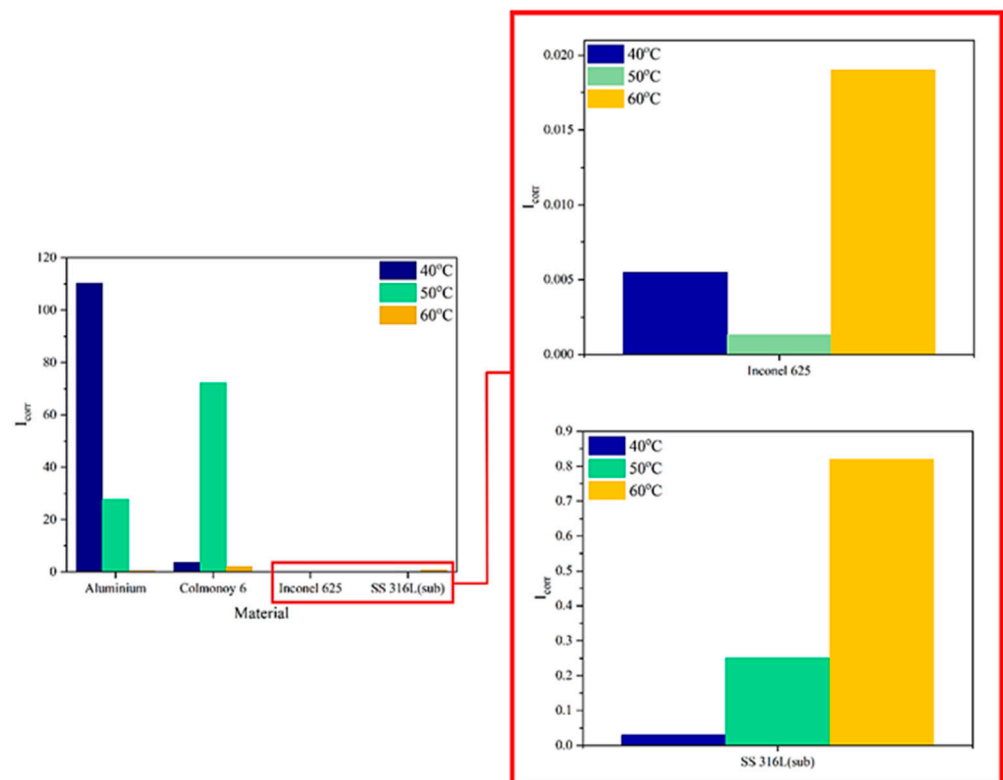

Figure 8. Potential of different coating samples at different temperatures.
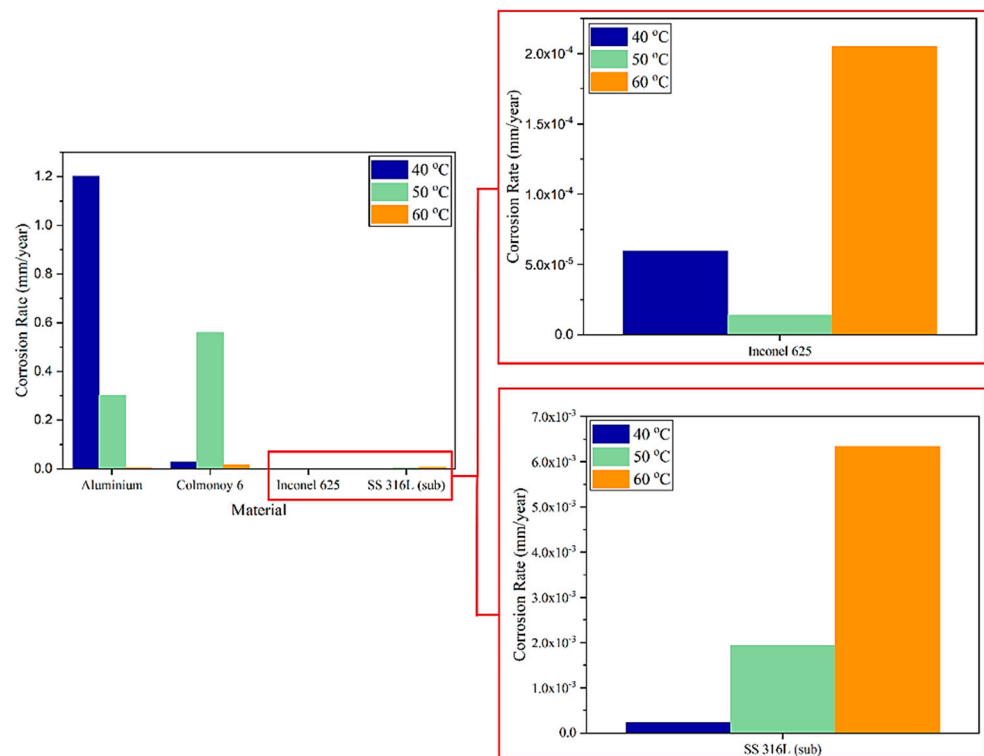
Figure 9. The corrosion rate of all coating samples at different temperatures.

3.2.2. Electrochemical Impedance Spectrometry (EIS)

The EIS investigations were conducted in 3.5% NaCl solution at 40, 50, and 60 °C under the OCP condition to obtain further details about the corrosion mechanisms. Figure 10 depicts the Nyquist, bode, and bode phase diagrams at specified temperatures. The Brug formulas were used to obtain capacitance values from CPE parameters in this study [29]. The impedance values of CPE and CPE are defined as below [30]:

$$Z_{CPE} = 1/(Q(\omega \cdot i)^{-n}) \tag{2}$$

$$CPE = (QR^{1-n})^{(1/n)} \tag{3}$$

where Z_{CPE} is the CPE impedance, Q is the CPE constant, ω is the angular frequency, R is the parallel resistor with CPE in the equivalent circuit, and i is the imaginary unit. In these equations, n is a number that represents surface inhomogeneity. The value of n can range from −1 to 1, where 1 represents an ideal capacitor, −1 represents a pure inductor, and 0 represents a perfect resistor.

Figure 10a,b shows the Nyquist and bode plot belonging to the Colmonoy coating at 40 °C. The Colmonoy-coated sample's Nyquist diagram is a semi-loop with a single CPE, indicating capacitance behavior associated with NiO formation. This P-type semiconductor layer functions as a barrier, retarding the corrosive ion's movements toward the substrate surface. The γ-Ni phase is the phase typical in both Inconel and Colmonoy, causing similar corrosion behaviors in both samples. However, the SEM results show intermetallic compounds in the coating, seen as discontinuous gray splats, deteriorating the corrosion resistance of the coating [30].

The bode diagram in Figure 10b indicates two constant phase elements in Inconel-coated samples. The Nyquist diagram in Figure 10a confirms the presence of two layers, given the two semi-loops seen in the curve. The first CPE in low frequencies refers to the layer formed at the solution/coating interface (NiO), with the second CPE in high frequencies being related to the Cr_2O_3 oxide layer. The calculated resistance value for the nickel oxide layer in Table 4 is 304 $\Omega \cdot cm^2$, much lower than the second layer (197,990 $\Omega \cdot cm^2$),

which indicates that the NiO layer does not show adequate resistance behavior. The second layer improves the corrosion resistance by forming a layer with a higher density than the former passive layer (NiO), according to the high resistance number calculated in Table 4. Considering that higher impedance at lower frequencies in the bode plot indicates better corrosion resistance, the Inconel coating can be described as showing higher resistance than Colmonoy, thanks to the existence of Cr_2O_3 as a protective layer in the Inconel coating.
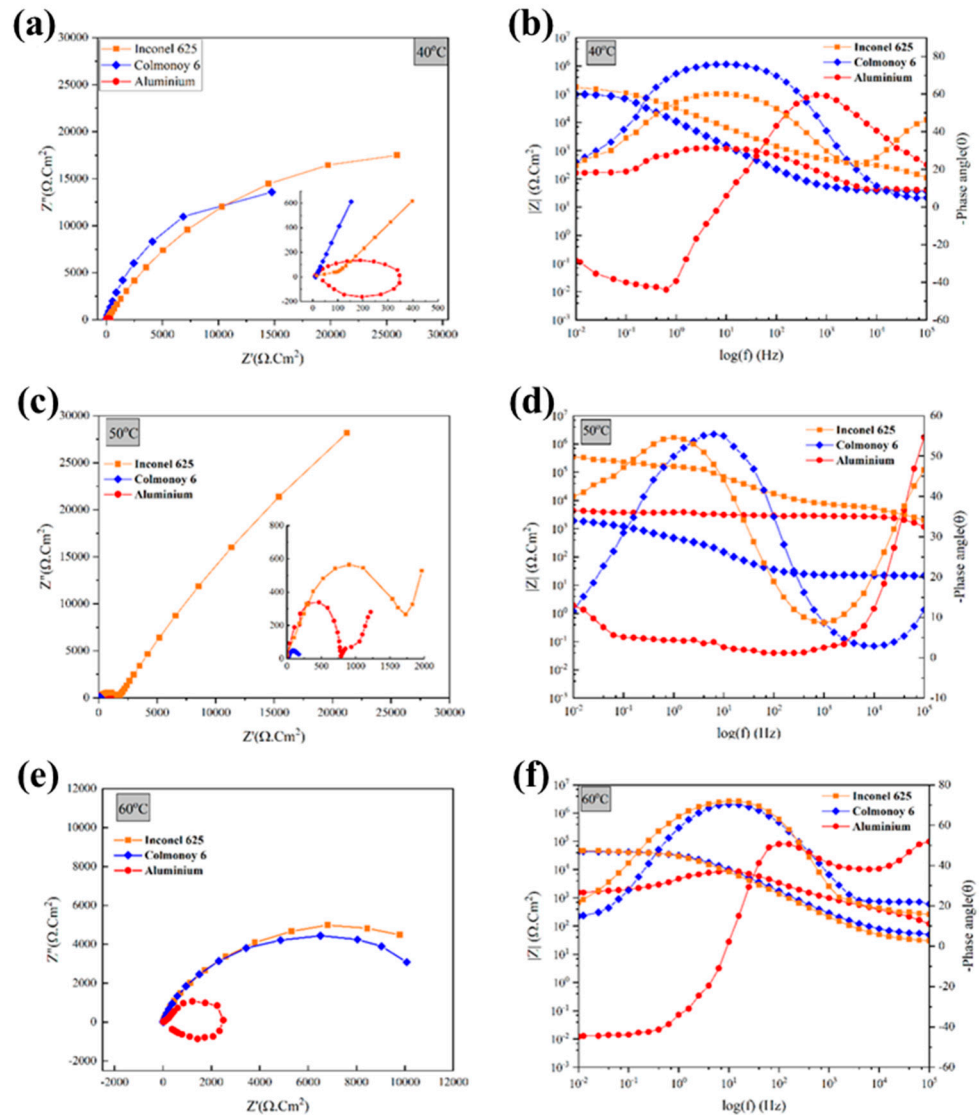

Figure 10. The EIS curves of the coatings at (**a,b**) 40 °C, (**c,d**) 50 °C, and (**e,f**) 60 °C.

Table 4. Impedance parameters results calculated for all coatings at 40 °C.

Parameter/Coating	Aluminum	Colmonoy-6	Inconel 625
RS ($\Omega \cdot cm^2$)	24.74	38	22.61
R1 ($\Omega \cdot cm^2$)	1269	130,450	304.1
CPE1 (F/cm^2)	5.6×10^{-6}	1.94×10^{-5}	2.67×10^{-7}
n1	0.82	0.85	0.789
R2 ($\Omega \cdot cm^2$)	-	-	197,990
CPE2 (F/cm^2)	-	-	7.8×10^{-6}
n1	-	-	0.71
L1 (S)	208	-	-
RL ($\Omega \cdot cm^2$)	119	-	-

Figure 10a illustrates the Nyquist diagram of an Al coating with an inductor loop due to a γ-Al_2O_3 oxide layer formed on the surface [31]. This layer is always present on the Al coating exposed to air and is hydrated in aqueous solutions. This hydrated layer reacts with the chloride ion in the solution as follows, resulting in pitting corrosion:

$$Al(OH)_3 + 3NaCl \rightarrow AlCl_3 + 3NaOH$$
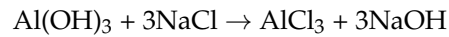
The creation of Al hydroxide causes a change in the pH of the solution, which causes this reaction [30]. Figure 11a depicts the equivalent circuits of the Colmonoy coating at 40 °C. Rs is the solution resistance, and CPE1 is the double-layer capacitance of the nickel oxide generated on the coating/solution surface as a result of the hydrolysis of the cations released from the coating [32]. R_c represents the charge transfer resistance of the double layer. Similarly, in the equivalent circuit of Inconel coating at 40 °C shown in Figure 11b, Rs is the solution resistance, R1 is the charge transfer resistance of the nickel oxide layer generated on the coating/solution interface, and CPE1 is the double-layer capacitance of this layer. R2 refers to the dense oxide layer (Cr_2O_3) generated on the sublayer surface during the coating process, which has a high corrosion resistance according to the results (197,990 Ω cm^2) reported in Table 4, and CPE2 is the double-layer capacitance of this layer in the substrate/coating interface. Similarly, for the Al coating, L1 is the inductor parameter associated with a kinetic impedance in Figure 11c, R1 is the charge transfer resistance of the layer, and CPE1 is the double-layer capacitance of the passive layer formed at the interface. The corrosion parameters were computed by Formula 3 using Z-View software for three coatings at 40 °C and are tabulated in Table 4.
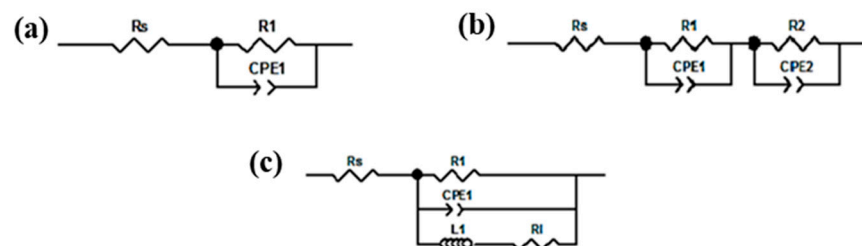

Figure 11. Equivalent circuits of (**a**) Colmonoy, (**b**) Inconel, and (**c**) Al coatings at 40 °C.

Figure 10c,d shows the results of the Bode and Nyquist plots of the samples at 50 °C. The existence of a CPE can be seen in the bode diagram of the Colmonoy coating at 50 °C, which is confirmed by the loop in the Nyquist diagram. The loop's small radius shows that the coating corroded quickly. The solubility of oxygen at this temperature is most likely the cause of the observed phenomenon. It is known that the solubility of oxygen reduces as the temperature rises. Because oxygen solubility is a vital component in creating the oxide layer, the oxide layer's recovery is limited at high temperatures. Moreover, the diffusion of chloride ions increases as the temperature goes up, which intensifies the corrosion of the coating at 50 °C.

Figure 10c,d shows the results of the Bode and Nyquist plots of the samples at 50 °C. The existence of a CPE can be seen in the bode diagram of the Colmonoy coating at 50 °C, which is confirmed by the loop in the Nyquist diagram. The loop's small radius shows that the coating corroded quickly. The solubility of oxygen at this temperature is most likely the cause of the observed phenomenon. This behavior can be attributed to an oxide layer, Cr_2O_3, inhibiting the chlorine ions from penetrating through the coating. Furthermore, corrosion products of this oxide act as an extra barrier against penetration by filling the surface cracks and preventing corrosive ions from penetrating the substrate [33,34]. The chromium oxide layer in the coating itself is responsible for the high corrosion resistance, despite accelerating the movement of corrosive ions with rising temperature.

The Nyquist diagram of Al coating at 50 °C is shown in Figure 10c. Nonetheless, Al-coated samples reveal a tri-loop, implying the formation of an $Al(OH)_3$ porous layer along with a passive Al_2O_3 layer based on the reactions shown below [29]:

$$Al_{(s)ads} + 3OH^- = Al(OH)_{3,ads} + 3e^-$$

$$2Al(OH)_{3,ads} = Al_2O_3 \cdot 3H_2O$$
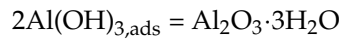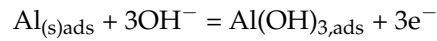
However, the EIS test results are not perfectly consistent with the Tafel test results in this case. Tafel test findings showed no evidence of creating a passive layer, while Nyquist plot results indicated that passive layers form in Al-coated materials. This could be the reason for the Al ion's quick interaction with the existing chlorine ions to generate $AlCl_4^-$, which degrades the protective layer [35,36].

The reason behind the varied behavior of Al-coated samples at different temperatures is that Al corrosion is dependent on multiple parameters (besides the oxide layer) at the same time: (i) the oxygen diffusion rate increases with the temperature, while (ii) the solubility of oxygen decreases as the temperature rises. Corrosion resistance improves at 50 °C due to $Al(OH)_3$ layer formation. The ability to build and restore the layer to improve corrosion resistance is enabled at this temperature due to the increased penetration of oxygen ions at higher temperatures. However, the presence of hard and brittle corrosion products of $Al(OH)_3$ reduces the corrosion resistance of this coat, so the corrosion resistance is not as much as expected.

Figure 12a depicts the equivalent circuit for the Colmonoy coating at 50 °C. In this figure, Rs is the electrolyte solution resistance, CPE1 denotes the coating/solution interface double-layer capacitance, and R1 indicates the charge transfer resistance of this layer. Comparing the values of R1 and CPE1 in Tables 4 and 5, it is evident that the Colmonoy coating has a lower corrosion resistance at this temperature. In Figure 12b, depicting the equivalent circuit for an Inconel-coated specimen, Rs denotes the electrolyte solution resistance, and CPE1 is the constant phase element of the oxide layer at the coating/solution interface (nickel oxide). The corrosion resistance of this layer generated on the surface is lower than that of the second oxide layer, i.e., the chromium oxide. The Cr_2O_3 layer has a high resistance characteristic according to CPE and R numbers calculated in Table 5. Furthermore, CPE2 is related to the substrate/oxide (Cr_2O_3) interface (double-layer capacitance), with R2 being the charge transfer resistance of this layer. Resistance values higher than the 40 °C samples imply an increased charge transfer resistance enhancing corrosion resistance. According to the Nyquist diagram, there is a penetration mechanism in the performance of the Inconel coating. This finding follows the EDX results, showing no penetration, and the sample has only capacitive behavior.
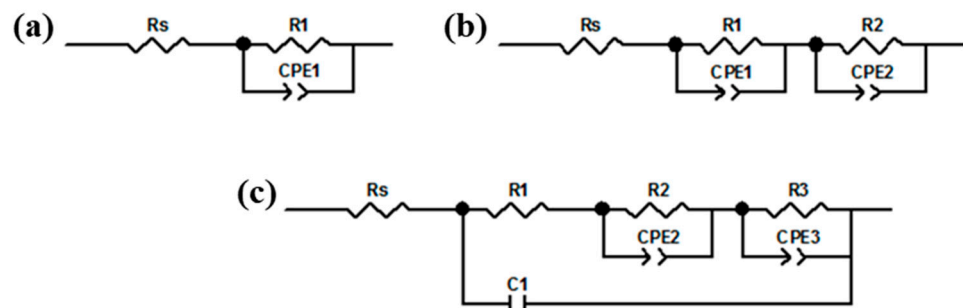

Figure 12. Equivalent circuits of (**a**) Colmonoy, (**b**) Inconel, and (**c**) Al coatings at 50 °C.

Table 5. Impedance parameters results calculated for all coatings at 50 °C.

Parameter/Coating	Aluminum	Colmonoy-6	Inconel 625
R_S ($\Omega \cdot cm^2$)	239	26.26	178
R_1 ($\Omega \cdot cm^2$)	2492	617.8	5833
CPE_1 (F/cm^2)	5.6×10^{-6}	9.11×10^{-5}	2.1×10^{-8}
n1	0.82	0.65	0.75
R2 ($\Omega \cdot cm^2$)	19,703	-	830,690
CPE2 (F/cm^2)	4.9×10^{-3}	-	3.99×10^{-6}
n_2	0.64	-	0.71
R3	1017	-	-
CPE3 (F/cm^2)	4.7×10^{-4}	-	-
n_3	0.54	-	-
C1 (F/cm^2)	1.4×10^{-9}	-	-

The equivalent circuit of the Al coating is shown in Figure 12c, where Rs represents the electrolyte solution resistance, R1 represents the charge transfer resistance of $Al(OH)_3$, and C1 represents its capacity obtained from Z-View software. CPE2 is the double-layer capacitance of the Al_2O_3 layer, while R1 is the charge transfer resistance of the coating. The double-layer capacitance of the Al_2O_3/substrate interface is CPE3, and the charge transfer resistance of the layer is R3. Impedance parameters calculated for all coatings at 60 °C are shown in Table 6.

Table 6. Impedance parameters results calculated for all coatings at 60 °C.

Parameter/Coating	Aluminum	Colmonoy-6	Inconel 625
Rs ($\Omega \cdot cm^2$)	20.77	49.94	31.49
R1 ($\Omega \cdot cm2$)	829	43,350	29.45
CPE1 (F/cm^2)	6.59×10^{-7}	2.13×10^{-5}	-
n_1	0.71	0.79	-
R2 ($\Omega \cdot cm^2$)	8008	-	48,965
CPE2 (F/cm^2)	6.86×10^{-7}	-	3.44×10^{-5}
n_2	0.88	-	0.74
L1 (S)	1410	-	-
RL ($\Omega \cdot cm^2$)	1894	-	-
C1 (F/cm^2)	-	-	5.68×10^{-6}

The Nyquist and bode plots of three coatings at 60 °C are shown in Figure 10e,f. The Colmonoy bode diagram (Figure 10f) depicts the presence of a CPE on the coating/solution surface, which is due to the formation of the Cr_2O_3 layer. The Nyquist diagram also confirms the existence of an unfinished loop (Figure 10e). Increasing temperature increases the penetration of oxygen ions, escalating the possibility of Cr_2O_3 layer formation and improving corrosion resistance due to its inhibitory properties. The migration of chlorine ions increases at this temperature, but the inhibitory effect of Cr_2O_3 improves the sample's corrosion resistance.

The bode diagram of the Inconel sample features two CPEs. The C1 is caused by forming a passive Cr_2O_3 layer, whereas CPE_2 represents a double-layer capacitance at the sublayer/Cr_2O_3 interface. There is just one layer (Cr_2O_3) since NiO cannot form at this temperature. An open inductor loop was also seen at a low frequency for the Al sample (Figure 10e), indicating pitting corrosion and an Al oxide layer on the surface. The creation of the $Al(OH)_3$ layer is significantly influenced by temperature; however, chlorine ion penetration increases as temperature rises, making it challenging to have $Al(OH)_3$ as a layer.

Figure 13a depicts the Colmonoy coating's equivalent circuit at 60 °C. CPE1 is the double-layer capacitance of the chromium oxide layer formed on the coating/solution interface, R1 is the charge transfer resistance of that layer, and Rs is the resistance of the electrolyte solution. In the Inconel coating (Figure 13b), Rs is electrolyte solution resistance,

C1 is the capacitance of the Cr_2O_3 layer, R1 is the resistance of this layer formed on the electrolyte/coating interface, CPE2 is the double-layer capacitance formed in Cr_2O_3/sublayer interface, and R2 is the charge transfer resistance of this layer. Figure 13c depicts the equivalent circuit of the Al coating at 60 °C, where CPE1 is the double-layer capacitance of the Al_2O_3 layer at the coating/solution interface, R1 is the charge transfer resistance of the layer, L1 is the inductor parameter of Al_2O_3, and RL is indicative of severe corrosion for this layer. CPE2 is the double-layer capacitance of corrosion products such as $AlCl_3$ in the substrate/coating interface, and R2 is the charge transmission resistance of this layer. The effective capacitance and thickness of the double layer for all coatings in different temperatures are listed in Table 7.
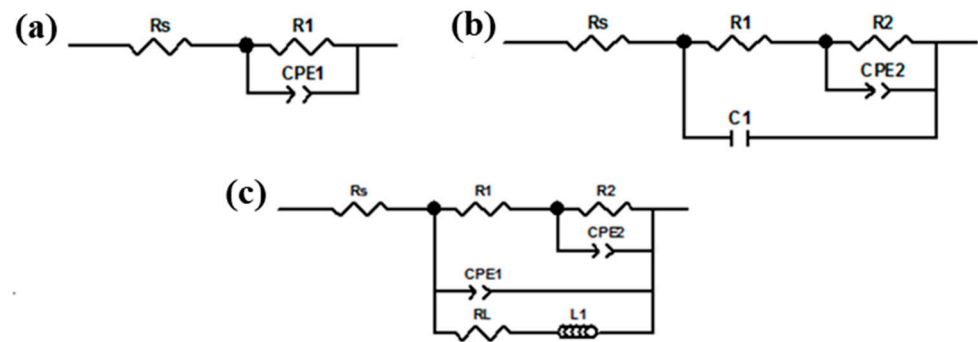

Figure 13. Equivalent circuits of (**a**) Colmonoy, (**b**) Inconel, and (**c**) Al coatings at 60 °C.

Table 7. The effective capacitance and thickness of the double layer.

Coating	C_{eff} (F)	D_{eff} (nm)
Colmonoy-6 at 40 °C	2.2854×10^{-5}	3.099322355
Colmonoy-6 at 50 °C	1.93481×10^{-5}	3.660924922
Colmonoy-6 at 60 °C	2.08533×10^{-5}	3.396688246
Inconel at 40 °C	0.931504×10^{-5}	7.604046969
Inconel at 50 °C	0.0650932×10^{-5}	10.8816314
Inconel at 60 °C	4.13162×10^{-5}	1.714389846
Aluminum at 40 °C	0.018906×10^{-5}	37.46541771
Aluminum at 50 °C	25.0617×10^{-5}	0.282630695
Aluminum at 60 °C	$0.00337382 \times 10^{-5}$	209.9461475

The C_{eff} was calculated by Equation (4), where C_{eff} is effective capacitance, Q is the constant of CPE, α is between 0 and 1, and R is the film resistance [37]:

$$C_{eff} = Q^{(1/\alpha)} R^{((1-\alpha)/\alpha)} \tag{4}$$

By C_{eff}, the double-layer thickness was gained by Equation (5):

$$C_{eff} = (\varepsilon \cdot \varepsilon_0)/d \tag{5}$$

where ε is the dielectric constant of 3.5% NaCl solution (=80), and $\varepsilon_0 = 8.854 \times 10^{-14}$ is the permittivity of vacuum [38]. The parameters yielded by Equations (4) and (5) are listed in Table 4.

4. Conclusions

The use of HVOF technology has been dramatically increasing in different industrial sectors, such as oil, gas, and petrochemical industries. HVOF coatings are often known to have high wear and corrosion resistance. In addition, the HVOF technology has been shown to be a promising alternative for electroplating because it produces low-porosity adherent coatings. Additionally, contrary to plating techniques, HVOF coatings show

hardly any continuous network of micro-cracks. Micro-cracks can provide routes for the penetration of electrolytes and can also weaken the mechanical properties of the coating. In the HVOF process, the interaction time between the powder and the flame is rather short. Furthermore, the high kinetic energy at the powder/substrate interface ends up in cohesion at the coating/substrate interface. However, depending on the HVOF conditions and the type of powder, different intermetallic phases can exist in the final structure. Moreover, oxidation at high temperature at the surface is expected to take place. The corrosion behavior of HVOF-sprayed coatings is rather complex because of their multiphase microstructure, which creates multi-corrosion cell locations, such as interlayer boundaries, phase boundaries, pores, oxide inclusions, and non-uniform dissolution reactions at the boundaries. These microstructural features intensely influence the corrosion mechanisms. One can expect that these mentioned interfaces are all active corrosion sites. Furthermore, it is highly likely that the coating possesses some inter-linked porosities. The presence of porosities and micro-cracks is critical when corrosion resistance is the main concern. Interconnected porosities are suitable places for the penetration of electrolytes towards the substrate. Depending on the activity of the coating compared to the substrate, galvanic corrosion reactions can take place at the interface. With that postulated, it is not a surprise that Inconel, comprising a rather continuous in-between-layers chromium oxide, can significantly enhance corrosion resistance. Cr is known to be influential in the corrosion resistance of HVOF coatings, as the Cr oxide layer can act as a barrier against electrolyte penetration. This work tends to compare three different industrial HVOF coatings. Three coatings of Al, Inconel, and Colmonoy were applied on the stainless steel substrate by the HVOF process. The microstructures of coated specimens were characterized by optical and electron microscopes. Corrosion behaviors of the coatings at three temperatures of 40, 50, and 60 °C were also studied, using electrochemical impedance and Tafel tests. The obtained results are summarized below:

1. The microstructure characterizations and phase analyses indicated that the powders were melted entirely in Al-coated specimens, and the coating was uniform. At the same time, in Inconel-coated samples, a lamella structure was evident, with oxide layers forming in between splats. In the Colmonoy coating, the splats were evident due to the partial melting of the Colmonoy particles during deposition. SEM micrographs showed that the three coatings were homogeneous, with hardly any discontinuity or cracks.

2. The polarization and EIS test results showed that overall, the Al coating showed the worst corrosion behavior, and the Inconel coating showed the best corrosion behavior. The Al-coated samples had the lowest oxidation/reduction potential of the coatings, indicating that HVOF Al-coated specimens undergo severe corrosion in experimental conditions. It appears that in the Inconel coating, the presence of Cr_2O_3 layers in between the lamella structure of the coating prevents the chlorine ions' diffusion, and this in turn significantly lowers the corrosion rate of Inconel-coated specimens.

3. At 40 °C and 50 °C, the Inconel coating has the highest corrosion resistance among the examined samples, and Al has the lowest corrosion resistance. Although there are three loops in the Nyquist curve of the Al coating, inferring the formation of oxide layers, the Tafel test results indicate that severe corrosion occurs. This was explained by the formation of $AlCl_4{}^-$ and the removal of the passive layer from the surface.

4. At 60 °C, the corrosion resistance of all coatings is comparatively lower than at the other two testing temperatures. This can be explained by the higher the temperature, causing higher diffusion and greater mobility of chlorine and other ions, making the corrosion kinetics faster.

5. The best corrosion performance was observed in Inconel-coated specimens at 50 °C.

References

1. Oladijo, O.P.; Luzin, V.; Maledi, N.B.; Setswalo, K.; Ntsoane, T.P.; Abe, H. Residual Stress and Wear Resistance of HVOF Inconel 625 Coating on SS304 Steel Substrate. *J. Therm. Spray Technol.* **2020**, *29*, 1382–1395. [CrossRef]
2. Hou, X.; Ren, Q.; Yang, Y.; Cao, X.; Hu, J.; Zhang, C.; Deng, H.; Yu, D.; Li, K.; Lan, W. Effect of Temperature on the Electrochemical Pitting Corrosion Behavior of 316L Stainless Steel in Chloride-Containing MDEA Solution. *J. Nat. Gas Sci. Eng.* **2021**, *86*, 103718. [CrossRef]
3. Henry, P.; Takadoum, J.; Berçot, P. Depassivation of Some Metals by Sliding Friction. *Corros. Sci.* **2011**, *53*, 320–328. [CrossRef]
4. Zhang, L.; Tang, X.; Wang, Z.; Li, T.; Zhang, Z.; Lu, M. The Corrosion Behavior of 316L Stainless Steel in H2S Environment at High Temperatures. *Int. J. Electrochem. Sci.* **2017**, *12*, 8806–8819. [CrossRef]
5. Ding, J.; Zhang, L.; Lu, M.; Wang, J.; Wen, Z.; Hao, W. The Electrochemical Behaviour of 316L Austenitic Stainless Steel in Cl− Containing Environment under Different H2S Partial Pressures. *Appl. Surf. Sci.* **2014**, *289*, 33–41. [CrossRef]
6. Einziger, R.E.; Tsai, H.C.; Billone, M.C.; Hilton, B.A.; Falls, I.; Power, V.; Nuclear, S.; Pressurized, S.; Storage, D.; Examination, F. In Proceedings of the 10th International Conference on Nuclear Engineering, Arlington, VA, USA, 14–18 April 2017; pp. 1–8.
7. Tani, J.; Mayuzumi, M.; Hara, N. Stress Corrosion Cracking of Stainless-Steel Canister for Concrete Cask Storage of Spent Fuel. *J. Nucl. Mater.* **2008**, *379*, 42–47. [CrossRef]
8. Sander, G.; Cruz, V.; Bhat, N.; Birbilis, N. On the In-Situ Characterisation of Metastable Pitting Using 316L Stainless Steel as a Case Study. *Corros. Sci.* **2020**, *177*, 109004. [CrossRef]
9. Tsutsumi, Y.; Nishikata, A.; Tsuru, T. Pitting Corrosion Mechanism of Type 304 Stainless Steel under a Droplet of Chloride Solutions. *Corros. Sci.* **2007**, *49*, 1394–1407. [CrossRef]
10. Dhaiveegan, P.; Elangovan, N.; Nishimura, T.; Rajendran, N. Corrosion Behavior of 316L and 304 Stainless Steels Exposed to Industrial-Marine-Urban Environment: Field Study. *Rsc Adv.* **2016**, *6*, 47314–47324. [CrossRef]
11. Evangeline, A.; Sathiya, P. Cold Metal Arc Transfer (CMT) Metal Deposition of Inconel 625 Superalloy on 316L Austenitic Stainless Steel: Microstructural Evaluation, Corrosion and Wear Resistance Properties. *Mater. Res. Express* **2019**, *6*, 066516. [CrossRef]
12. Kwok, C.T.; Man, H.C.; Cheng, F.T. Cavitation Erosion and Pitting Corrosion of Laser Surface Melted Stainless Steels. *Surf. Coatings Technol.* **1998**, *99*, 295–304. [CrossRef]
13. Wang, Y.; Hao, E.; An, Y.; Hou, G.; Zhao, X.; Zhou, H. The Interaction Mechanism of Cavitation Erosion and Corrosion on HVOF Sprayed NiCrWMoCuCBFe Coating in Artificial Seawater. *Appl. Surf. Sci.* **2020**, *525*, 146499. [CrossRef]
14. Boudi, A.A.; Hashmi, M.S.J.; Yilbas, B.S. HVOF Coating of Inconel 625 onto Stainless and Carbon Steel Surfaces: Corrosion and Bond Testing. *J. Mater. Process. Technol.* **2004**, *155–156*, 2051–2055. [CrossRef]
15. Verdian, M.M.; Raeissi, K.; Salehi, M. Electrochemical Impedance Spectroscopy of HVOF-Sprayed NiTi Intermetallic Coatings Deposited on AISI 1045 Steel. *J. Alloys Compd.* **2010**, *507*, 42–46. [CrossRef]
16. Oliveira, F.; Hernandez, L.; Berríos, J.A.; Villalobos, C.; Pertuz, A.; Cabrera, E.S.P. Corrosionfatigue Properties of a 4340 Steel Coated with Colmonoy 88 Alloy, Applied by HVOF Thermal Spray. *Surf. Coat. Technol.* **2001**, *140*, 128–135. [CrossRef]
17. Verdian, M.M.; Raeissi, K.; Salehi, M. Corrosion Performance of HVOF and APS Thermally Sprayed NiTi Intermetallic Coatings in 3.5% NaCl Solution. *Corros. Sci.* **2010**, *52*, 1052–1059. [CrossRef]
18. Gil, L.; Staia, M.H. Influence of HVOF Parameters on the Corrosion Resistance of NiWCrBSi Coatings. *Thin Solid Films* **2002**, *420*, 446–454. [CrossRef]
19. Kim, I.-K.; Hong, S.I. Effect of Heat Treatment on the Bending Behavior of Tri-Layered Cu/Al/Cu Composite Plates. *Mater. Des.* **2013**, *47*, 590–598. [CrossRef]
20. Liu, H.; Tan, C.K.I.; Meng, T.L.; Teo, S.L.; Liu, J.; Cao, J.; Wei, Y.; Tan, D.C.C.; Lee, C.J.J.; Suwardi, A.; et al. Hot Corrosion and Internal Spallation of Laser-Cladded Inconel 625 Superalloy Coatings in Molten Sulfate Salts. *Corros. Sci.* **2021**, *193*, 109869. [CrossRef]
21. Karmakar, R.; Maji, P.; Ghosh, S.K. A Review on the Nickel Based Metal Matrix Composite Coating. *Met. Mater. Int.* **2021**, *27*, 2134–2145. [CrossRef]

22. Dadfar, M.; Fathi, M.H.; Karimzadeh, F.; Dadfar, M.R.; Saatchi, A. Effect of TIG Welding on Corrosion Behavior of 316L Stainless Steel. *Mater. Lett.* **2007**, *61*, 2343–2346. [CrossRef]
23. Han, Y.; Zhu, Z.; Zhang, B.; Chu, Y.; Zhang, Y.; Fan, J. Effects of Process Parameters of Vacuum Pre-Oxidation on the Microstructural Evolution of CoCrAlY Coating Deposited by HVOF. *J. Alloys Compd.* **2018**, *735*, 547–559. [CrossRef]
24. Yung, T.Y.; Chen, T.C.; Tsai, K.C.; Lu, W.F.; Huang, J.Y.; Liu, T.Y. Thermal Spray Coatings of Al, ZnAl and Inconel 625 Alloys on SS304L for Anti-Saline Corrosion. *Coatings* **2019**, *9*, 32. [CrossRef]
25. Yang, J.; Bai, S.; Sun, J.; Wu, H.; Sun, S.; Wang, S.; Li, Y.; Ma, W.; Tang, X.; Xu, D. Microstructural understanding of the oxidation and inter-diffusion behavior of Cr-coated Alloy 800H in supercritical water. *Corros. Sci.* **2023**, *211*, 110910. [CrossRef]
26. Cao, M.; Liu, L.; Fan, L.; Yu, Z.; Li, Y.; Oguzie, E.E.; Wang, F. Influence of Temperature on Corrosion Behavior of 2A02 Al Alloy in Marine Atmospheric Environments. *Materials* **2018**, *11*, 235. [CrossRef] [PubMed]
27. Zhang, L.; Hu, Z.; Huang, J.; Chen, Z.; Li, X.; Feng, Z.; Yang, H.; Huang, S.; Luo, R. Experimental and DFT studies of flower-like Ni-doped Mo_2C on carbon fiber paper: A highly efficient and robust HER electrocatalyst modulated by $Ni(NO_3)_2$ concentration. *J. Adv. Ceram.* **2022**, *11*, 1294–1306. [CrossRef]
28. Zhang, L.; Huang, J.; Hu, Z.; Li, X.; Ding, T.; Hou, X.; Chen, Z.; Ye, Z.; Luo, R. $Ni(NO_3)_2$-induced high electrocatalytic hydrogen evolution performance of self-supported fold-like WC coating on carbon fiber paper prepared through molten salt method. *Electrochim. Acta* **2022**, *422*, 140553. [CrossRef]
29. Brug, G.J.; van den Eeden, A.L.G.; Sluyters-Rehbach, M.; Sluyters, J.H. The Analysis of Electrode Impedances Complicated by the Presence of a Constant Phase Element. *J. Electroanal. Chem. Interfacial Electrochem.* **1984**, *176*, 275–295. [CrossRef]
30. Stansbury, E.E.; Buchanan, R.A. *Fundamentals of Electrochemical Corrosion*; ASM International: Cleveland, OH, USA, 2000; ISBN 1615030670.
31. Jingling, M.A.; Jiuba, W.; Gengxin, L.I.; Chunhua, X.V. The Corrosion Behaviour of Al–Zn–In–Mg–Ti Alloy in NaCl Solution. *Corros. Sci.* **2010**, *52*, 534–539. [CrossRef]
32. Sabzi, M.; Mersagh Dezfuli, S. Deposition of Al_2O_3 Ceramic Film on Copper-based Heterostructured Coatings by Aluminizing Process: Study of the Electrochemical Responses and Corrosion Mechanism of the Coating. *Int. J. Appl. Ceram. Technol.* **2019**, *16*, 195–210. [CrossRef]
33. Raj, X.J. Investigation into the Effect of Cr_2O_3 Nanoparticles on the Protective Properties of Epoxy Coatings on Carbon Steel in 3.5% NaCl Solution by Scanning Electrochemical Microscopy. *Prot. Met. Phys. Chem. Surf.* **2019**, *55*, 80–88. [CrossRef]
34. Bahramian, A.; Eyraud, M.; Vacandio, F.; Hornebecq, V.; Djenizian, T.; Knauth, P. Single-Step Electrodeposition of Superhydrophobic Black NiO Thin Films. *J. Appl. Electrochem.* **2019**, *49*, 621–629. [CrossRef]
35. Xie, J.; Chen, Y.; Yin, L.; Zhang, T.; Wang, S.; Wang, L. Microstructure and mechanical properties of ultrasonic spot welding $TiNi/Ti_6Al_4V$ dissimilar materials using pure Al coating. *J. Manuf. Process.* **2021**, *64*, 473–480. [CrossRef]
36. Mujdrica Kim, M.; Kapun, B.; Tiringer, U.; Šekularac, G.; Milošev, I. Protection of Aluminum Alloy 3003 in Sodium Chloride and Simulated Acid Rain Solutions by Commercial Conversion Coatings Containing Zr and Cr. *Coatings* **2019**, *9*, 563.
37. Hirschorn, B.; Orazem, M.E.; Tribollet, B.; Vivier, V.; Frateur, I.; Musiani, M. Determination of Effective Capacitance and Film Thickness from Constant-Phase-Element Parameters. *Electrochim. Acta* **2010**, *55*, 6218–6227. [CrossRef]
38. McCafferty, E. *Introduction to Corrosion Science*; Springer Science & Business Media: Berlin, Germany, 2010; ISBN 1441904549.